Time-Scale and Sequence of Dynamic Structural Changes in a MgO-Attached Ruthenium Cluster Catalyst Observed by in Situ Time-Resolved DXAFS

Akane Suzuki,[†] Aritomo Yamaguchi,[‡] Teiji Chihara,[§] Yasuhiro Inada,[||] Makoto Yuasa,[‡] Masahiko Abe,[‡] Masaharu Nomura,[⊥] and Yasuhiro Iwasawa*,[†]

Department of Chemistry, Graduate School of Science, University of Tokyo, Hongo, Bunkyo-ku, Tokyo, 113-0033, Japan, Faculty of Science and Technology, Tokyo University of Science, Noda, Chiba 278-8510, Japan, The Institute of Physical and Chemical Research, Wako, Saitama 351-01, Japan, Research Center for Materials Science, Nagoya University, Nagoya 464-8602, Japan, and Photon Factory, Institute of Materials Structure Science, KEK, Ibaraki 305-0801, Japan

Received: July 16, 2003; In Final Form: January 6, 2004

The structural transformations of a MgO-attached [Ru_6C] cluster catalyst during carbonylation under CO/H_2 and decarbonylation under vacuum were studied by energy-dispersive X-ray absorption fine structure (DXAFS). The DXAFS study revealed that the carbonylation of [Ru_6C]/MgO to [$Ru_6C(CO)_{11}$]/MgO proceeded via two intermediates with the same composition [$Ru_6C(CO)_6$] with different Ru−Ru bond distances (0.265 and 0.269 nm). First, six CO molecules coordinate to a [Ru_6C] framework, and second, the Ru−Ru length expands from 0.265 to 0.269 nm. Finally, five CO molecules coordinate to the [$Ru_6C(CO)_6$] cluster to produce [$Ru_6C(CO)_{11}$] species, where the Ru−Ru distance is further elongated to 0.271 nm. In the decarbonylation process, the [$Ru_6C(CO)_6$]/MgO is partially decarbonylated to form [$Ru_6C(CO)_{11}$]/MgO accompanied with a decrease of Ru−Ru length from 0.271 to 0.269 nm. Then the complete decarbonylation occurs to form [Ru_6C] species, keeping the Ru−Ru distance at 0.269 nm. Finally, the cluster framework shrinks to recover the original [Ru_6C]/MgO with the Ru−Ru distance of 0.265 nm. There were definite time lags between the first carbonylation and the cluster framework expansion (2−4 s, depending on the temperature) and between the last decarbonylation and the cluster framework shrinkage (3−5 min, depending on the temperature). The activation energies for the structural changes in the Ru cluster framework in every transformation step under CO/H_2 (423−523 K) and vacuum (573−623 K) were estimated by the time-resolved DXAFS analysis. This sort of study is the first to provide structural kinetics of catalytically active metal sites at oxide surfaces.

1. Introduction

Reaction kinetics of gas phase molecules and dynamic behavior of adsorbed molecules during catalysis of supported metal clusters and particles have been extensively studied to date. Despite the success of analyses of the molecular kinetics and behavior, little is known about the dynamic properties of a multiply bonded cluster framework in supported metal clusters such as the time scale of concerted structural changes of several metal atoms in a cluster at the surface and the sequence of the changes in metal−metal and metal−adsorbate bondings, which may be relevant to dynamic processes in catalysis. A reason for the lack of knowledge is due to few suitable techniques for in situ time-resolved structural characterization of active metal sites at surfaces, which has been a long-term challenge and a serious subject. Another reason is due to few examples of suitable metal clusters with well-defined structures dispersed on oxide surfaces with good catalytic performances.[1,2]

IR, resonance Raman, XRD, luminescence, and NMR have been applied to investigation of transient or short-lived species in a time-resolved mode. Only XRD can provide direct structural information on crystalline materials, but it cannot provide any information on noncrystalline or dispersed materials such as supported metal catalysts. Time-resolved X-ray absorption fine structure (XAFS) technique is powerful for study of dynamic structural changes of dispersed metals at surfaces. Two methods are used for time-resolved XAFS measurements: quick scanning XAFS (QXAFS)[3−15] and energy-dispersive XAFS (DXAFS).[16−42] The DXAFS technique has better time resolution capability (10−100 ms) than the QXAFS technique (typically, in seconds). Thus, in this study DXAFS has been applied to studies on structural changes of metal sites on oxide surfaces during reduction, oxidation, temperature programmed desorption, etc.[16−42]

We reported the unique catalysis of [Ru_6C] clusters on MgO for CO/H_2 conversion to oxygenated compounds such as methanol, formaldehyde, and dimethyl ether and a structural change of the cluster framework before and after the catalytic CO/H_2 reaction.[43,44] The catalysis is contrasted with that of conventional supported Ru catalysts, which produce hydrocarbons such as methane under the identical reaction conditions. When the [Ru_6C]/ MgO with Ru−Ru bonds at 0.265 nm was exposed to CO/H_2 reaction gases at 523 K, the cluster framework expanded and [$Ru_6C(CO)_{11}$]/MgO with Ru−Ru bonds at 0.271 nm formed, adsorbing 11 CO molecules per cluster. At low CO pressures or in a vacuum, the carbonylated [$Ru_6C(CO)_{11}$]/MgO was transformed back to the original shrunk [Ru_6C] framework, desorbing the CO adsorbates.

We have succeeded in monitoring time-dependent ruthenium-carbido cluster structures at a MgO surface in a molecular scale by DXAFS. The preliminary results were reported, summarizing

* Corresponding author. Fax: (+81) 3-5800-6892. E-mail: iwasawa@chem.s.u-tokyo.ac.jp.
[†] University of Tokyo.
[‡] Tokyo University of Science.
[§] Institute of Physical and Chemical Research.
[||] Nagoya University.
[⊥] Institute of Materials Structure Science.

10.1021/jp030854g CCC: $27.50 © 2004 American Chemical Society
Published on Web 04/13/2004

SCHEME 1: Preparation Steps for MgO-Supported Ruthenium-Carbide Clusters

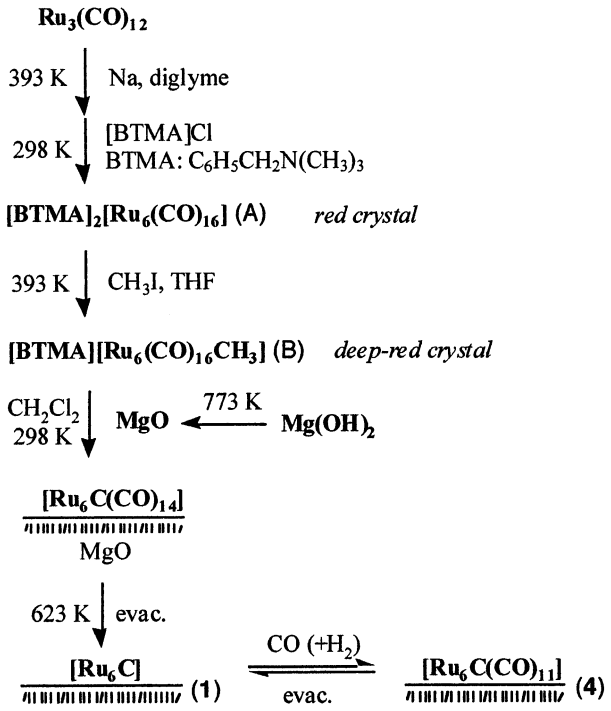

the information on how and when the cluster structure changes during the processes of CO adsorption and desorption.[41] This article reports novel issues such as the time scale and sequence of dynamic bond rearrangements in ruthenium-carbido clusters on MgO by DXAFS.

2. Experimental Section

2.1. Catalyst Preparation. Supported ruthenium-carbido clusters were prepared by the synthesis procedures reported previously as shown in Scheme 1. The synthesis procedures are briefly summarized here.[43−45] $Ru_3(CO)_{12}$, dry diglyme, and a piece of sodium were mixed and heated at 398 K until the sodium disappeared, followed by refluxing for 3 h. After removal of the solvent under reduced pressure, the residual viscous oil was dissolved in an aqueous solution of [BTMA]Cl and left overnight at 298 K. The red precipitate was filtered and purified by a silica gel column chromatograph (ethanol/acetone (1/1 v/v) elution), followed by recrystallization from ethanol/hexane to give red crystals of $[BTMA]_2[Ru_6C(CO)_{16}]$ (A). IR(CH_2Cl_2): $\tilde{\nu}$ (C═O) 2024 (w), 1976 (s), 1950 (sh,w), 1920 (m), and 1800 (m) cm^{-1}. The cluster (A) was dissolved into a solution of methyl iodide and THF. The solution was heated at 393 K for 1 h, and then it was evaporated under a reduced pressure. The residue was subjected to an alumina column chromatograph and eluted with dichloromethane. Crude crystals were obtained by evaporation of the red band. The recrystallization with *tert*-butyl alcohol/hexane gave deep-red crystals of $[BTMA][Ru_6C(CO)_{16}(CH_3)]$ (B). IR(CH_2Cl_2): $\tilde{\nu}$ (C═O) 2067 (w), 2045 (sh), 2014 (s), 1957(w), and 1800 (m) cm^{-1}.[43−45] The cluster (B) in CH_2Cl_2 was supported on MgO by reaction with OH groups of the surface (surface area: 105 $m^2\ g^{-1}$). The MgO was prepared from $Mg(OH)_2$ by calcination at 773 K for 2 h. The Ru loading was regulated to be 4.0 wt % as Ru/MgO. The obtained $[Ru_6C(CO)_{14}]$/MgO sample was evacuated at 623 K to give decarbonylated $[Ru_6C]$/MgO (**1**). The $[Ru_6C]$/MgO (**1**) can be reversibly transformed to $[Ru_6C(CO)_{11}]$/MgO (**4**) by exposure to CO/H_2 at 523 K.

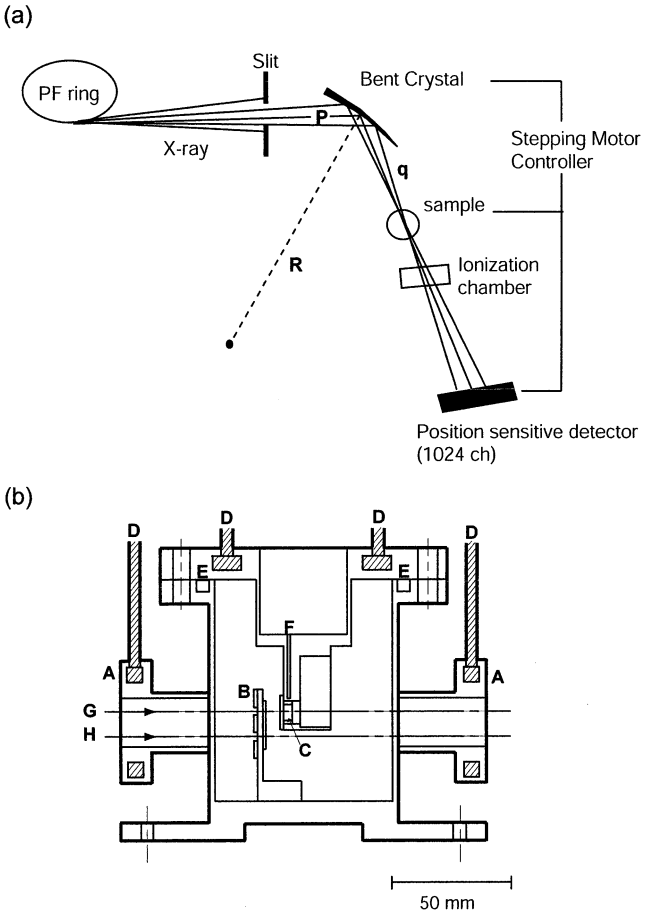

Figure 1. (a) DXAFS setup (Bragg case). $p = 30$ m, $q = 385$ mm, $R = 4.5$ m, $L = 36.2$ mm, $\theta_B = 9.9°$. The relationship for the curved polychromator is given by $1/p + 1/q = 2/(R \sin \theta_B)$. The energy range ($\Delta E$) is given by $\Delta E = E \cot \theta_B \Delta\theta = EL(1/4 - (\sin \theta_B)/p)\cot \theta_B$ where E, $\Delta\theta$, and L are the X-ray energy at the center of the crystal, the angular width of the Bragg angle θ_B, and the length of the irradiated crystal, respectively. (b) In situ DXAFS cell. A: Kapton window; B: slit; C: sample holder; D: cooling water pipe; E: O-ring; F: thermometer; G: X-ray for I; H: X-ray for I_0.

2.2. DXAFS Measurement. Energy dispersive XAFS (DXAFS) measurements were carried out at BL-9C of KEK-PF[29−31,34] with a Si(311) polychromator. A curved crystal, which is achieved by a triangle-shaped crystal clamped at its base and bent by a force applied to its apex, produces horizontal width of the X-rays at the focus point as shown in Figure 1a. We measured DXAFS spectra at Ru K-edge in the energy range of 21870−22920 eV under the conditions of p, q, R, L, and θ_B (see Figure 1a) being 30 m, 385 mm, 4.5 m, 36.2 mm and 9.9°, respectively. Because a cylindrical optics was used, the present setup gave a horizontal focus size of 1.0 mm, which agrees with a focus size of 0.9 mm calculated by the geometric configuration. In the Bragg configuration, XAFS amplitude at the Ru−K edge is distorted by asymmetric reflectivity profile,[46] but the EXAFS analysis for the $[Ru_6C]$/MgO catalysts was convincing enough, compared with that by conventional XAFS.

We designed an in situ DXAFS cell made from stainless steel as shown in Figure 1b. The cell was designed by the following strategy:

(1) Gas admission into the cell and evacuation of the gas from the cell can be operated outside the experimental hutch.

(2) It is possible to heat a sample to 773 K.

(3) To block stray lights, a slit is set before a sample.

(4) The measurement conditions for I (with sample) and I_0 (without sample) are controlled to be as equal as possible.

The catalyst 90 mg was pressed to a 7 mmϕ disk and placed at the sample holder in the cell. The sample thickness was regulated to show the edge jump was ca. 0.5. The in situ cell had two slits to measure I_0 and I. The sample in the in situ cell was placed on the X-ray focus point.

The diverging X-rays after the sample was detected by a position-sensitive detector, a photodiode array with 1024 sensing elements (0.025 mm wide, 2.5 mm high) manufactured by Hamamatsu Photonics (S3904-1024FX SPL3402). The energy calibration of each photodiode was carried out by comparing a DXAFS spectrum of Ru powder with a conventional XAFS spectrum measured with a Si(311) channel-cut monochromator at KEK-PF BL-10B. The second-order polynomial confirmed the quality of the DXAFS setup to be good enough for the EXAFS analysis.

A mixture of CO (26.7 kPa) and H_2 (26.7 kPa) was admitted to the sample maintained at a given temperature in the in situ cell within 10 ms by using a high-response gate valve. No effects of mass transfer and gas diffusivity on the DXAFS analysis were observed in our DXAFS system. The gas phase pressure did not change significantly because the Ru quantity was much less than the gas quantity. Reversely, the mixture of CO and H_2 was evacuated within 1 s. All the DXAFS spectra were measured in the in situ batch reactor cell in Figure 1b. The data acquisition time was 1 or 2 s for the carbonylation and decarbonylation processes, respectively.

2.3. Analysis of EXAFS. EXAFS data were analyzed by the UWXAFS package.[47] After background subtraction using AUTOBK,[48] k^3-weighted EXAFS functions were Fourier-transformed into *R*-space and fitted in the *R*-space. The backscattering amplitude and phase shift functions of Ru−Ru, Ru−(C)−O, Ru−C−(O), Ru−(C)−Ru, and Ru−O were calculated from [BTMA][$Ru_6C(CO)_{16}CH_3$] and RuO_2 by the FEFF8.0 code, and the curve fitting was done using the FEFFIT code.[49] The coefficient of the multiphoton reduction effects (S_0^2) was estimated to be 0.8 by fitting model compounds using the theoretical amplitude functions. The energy resolution of spectrometer (4.5 eV) was taken into account in the calculation of the parameters by using the "EXCHANGE" flag of an input file in the FEFF8.0 code. The number of independent parameters N_{idp} in the DXAFS analysis was restricted to be 11 by the Niquest formula.[50] The strategy to reduce the number of fitting parameters was to use the Debye−Waller factors of stable species calculated from conventional EXAFS data. Thus, the Debye−Waller factors were fixed at the values obtained by the curve-fitting analysis for the conventional EXAFS data measured at the same temperatures. The observed spectra were fitted by four shells, Ru−(C)−O and Ru−C−(O) of carbonyl ligands, Ru−Ru, and Ru−O. Because the coordination numbers (CNs) of Ru−C−(O) and Ru−(C)−O of carbonyl ligands should be equal, the number of the free parameters required for fitting the DXAFS data becomes eight, which is smaller than the N_{idp} (11).

2.4. FT-IR Measurement. In situ FT-IR spectra were measured on a JASCO FT-IR230 spectrometer. An IR cell with two NaCl windows was combined in a closed circulating system. The spectra were recorded as difference spectra with a 2 cm^{-1} resolution and about 24 s time acquisition by a single-beam method, where the spectra for a catalyst wafer were subtracted by the gas-phase spectra in a reference cell.

3. Results and Discussion

3.1. The Structural Parameters of [Ru_6C] Cluster. At first we measured conventional XAFS spectra for ([Ru_6C]/MgO (**1**)) and ([$Ru_6C(CO)_{11}$]/MgO (**4**)), which were analyzed by a curve-fitting technique. The results are shown in Table 1. The bond distance (*R*) and coordination number for Ru−Ru was 0.265 ± 0.001 nm and 4.2 ± 0.4, respectively. The [Ru_6C] cluster is suggested to have a distorted hexaruthenium framework because the Ru−(C)−Ru bond observed with the original [$Ru_6C(CO)_{16}CH_3$] cluster was not observed by EXAFS. The EXAFS intensity of the Ru−(C)−Ru peak is known to be reduced when the angle of Ru−C−Ru is different than 180°.[48] The Ru−O bond at the cluster−MgO interface was also observed at 0.200 ± 0.002 nm (CN: 1.1 ± 0.4). After CO/H_2 exposure at 523 K, the [Ru_6C]/MgO was transformed to [$Ru_6C(CO)_{11}$]/MgO, which showed the Rs (CNs) of Ru−Ru, Ru−C−(O), Ru−(C)−O, Ru−(C)−Ru, and Ru−O at 0.271 ± 0.001 (3.6 ± 0.6), 0.187 ± 0.002 (1.9 ± 0.3), 0.297 ± 0.003 (1.9 ± 0.3), 0.408 ± 0.006 (0.8 ± 0.3), and 0.208 ± 0.003 (1.0 ± 0.4) nm, respectively. The appearance of the Ru−(C)−Ru bond indicates recovery of the octahedral cluster framework. These parameters except the *R* of Ru−Ru bonds agree with those in our previous literature.[43] It was previously reported that the Ru−Ru distance increased from 0.263 for [Ru_6C]/MgO to 0.287 nm for [$Ru_6C(CO)_{11}$]/

TABLE 1: Structural Parameters for [Ru_6C]/MgO(1), [$Ru_6C(CO)_{11}$]/MgO(4), in the Carbonylation and Decarbonylation Processes Obtained by Conventional XAFS

abs.-scat	CN	R/0.1 nm	$\sigma^2/10^{-5}$ nm^2
Cluster (**1**) (523 K) ($\Delta E_0 = -3$ eV, $R_f = 1.5\%$, *R* range = 0.16−0.32 nm)			
Ru−Ru	4.2 ± 0.4	2.65 ± 0.02	10.9
Ru−O	1.1 ± 0.4	2.00 ± 0.02	13.9
Cluster (**4**) produced from (**1**) under CO/H_2 (523 K) ($\Delta E_0 = -6.1$ eV, $R_f = 5.0\%$, *R* range = 0.10−0.42 nm)			
Ru−Ru	3.6 ± 0.6	2.71 ± 0.01	13.4
Ru−C	1.9 ± 0.3	1.87 ± 0.02	7.6
Ru−(C)−O	1.9 ± 0.3	2.97 ± 0.03	8.0
Ru−O	1.0 ± 0.4	2.08 ± 0.03	14.9
Ru−C−Ru	0.8 ± 0.3	4.08 ± 0.06	11.1

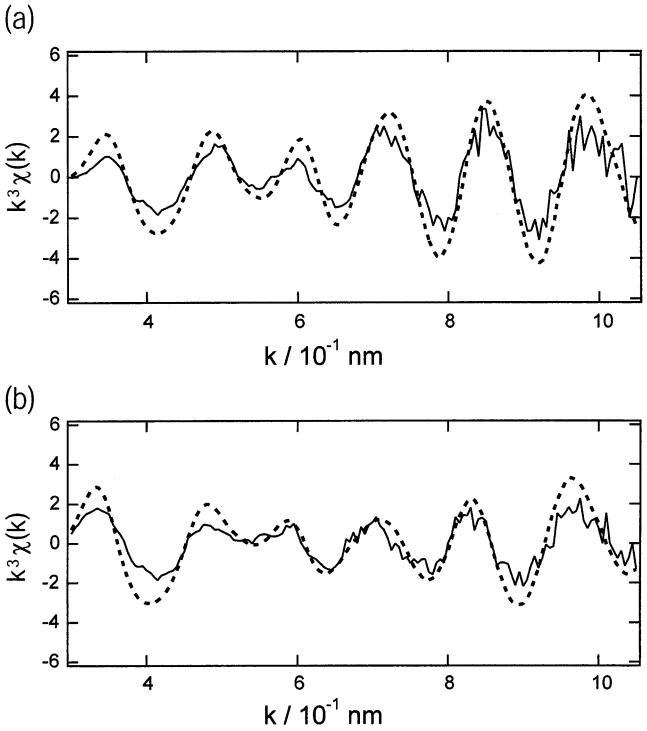

Figure 2. Typical k^3-weighted EXAFS functions for [Ru_6C]/MgO (a) and [$Ru_6C(CO)_{11}$]/MgO (b) measured by DXAFS(—) and conventional XAFS(- - -).

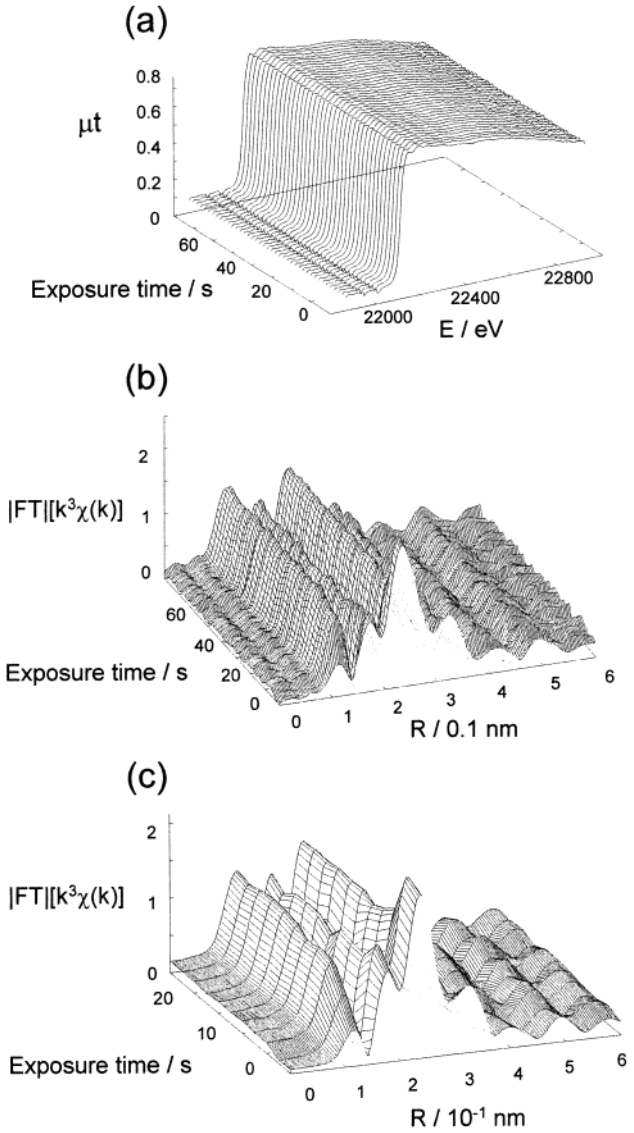

Figure 3. (a) A series of DXAFS spectra, (b) their Fourier-transformed functions, and (c) the Ru K-edge during the carbonylation of $[Ru_6C]$/MgO (**1**) under CO/H_2 (26.7 kPa/26.7 kPa) at 523 K. Cat. weight = 90 mg.

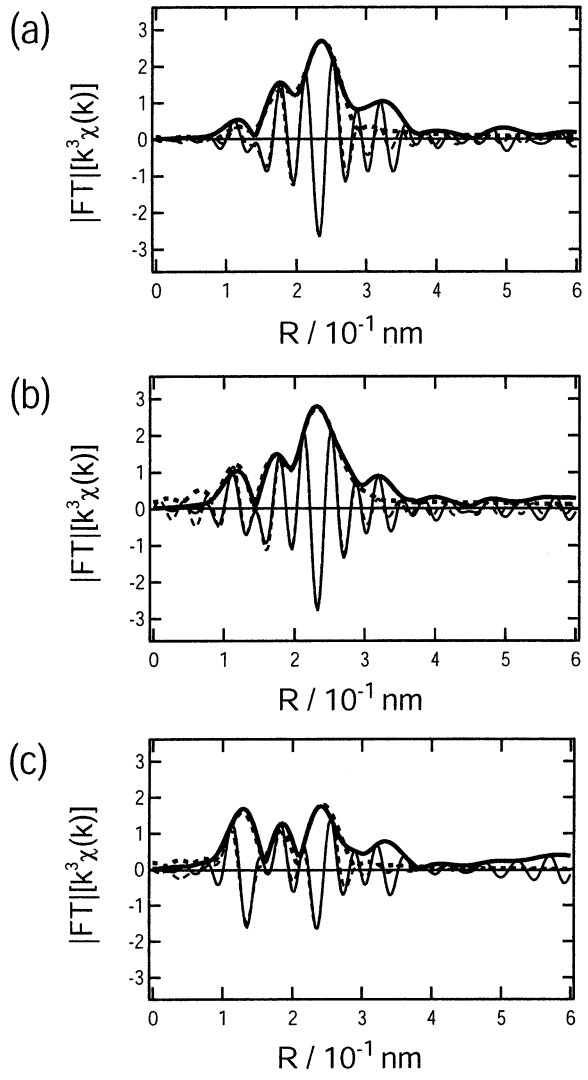

Figure 4. Fourier-transformed k^3-weighted EXAFS functions (—) and their imaginary parts (—) for $[Ru_6C]$/MgO (**1**) under CO/H_2 at 523 K measured by DXAFS, together with the curve fitting of the observed FT data (•••) and their imaginary parts (---). P_{CO} = 26.7 kPa; P_{H_2} = 26.7 kPa; Cat. weight = 90 mg. (a) 0 s (cluster (**1**)); (b) 2.1 s (intermediate cluster (**2**)); (c) 37.8 s (cluster (**4**)).

MgO, while in this study it increased from 0.265 to 0.271 nm. This disagreement may arise from the difference in the Ru loadings between 1.8 and 4.0 wt %. The transformation from $[Ru_6C(CO)_{11}]$/MgO back to $[Ru_6C]$/MgO occurred by evacuation at 523 K. As a consequence, the transformation between the shrunk cluster $[Ru_6C]$/MgO and the expanded cluster $[Ru_6C(CO)_{11}]$/MgO occurs reversibly as reported previously.[43−45]

Figure 2 shows the comparison of k^3-weighted EXAFS oscillations for $[Ru_6C]$/MgO (a) and $[Ru_6C(CO)_{11}]$/MgO (b) measured by DXAFS and conventional XAFS. The quality of the DXAFS spectra is reasonably good up to 100 nm^{-1}. The curve-fitting results for the DXAFS data are also shown in Table 1. The structural parameters determined by the DXAFS agree with those determined by the conventional XAFS. On the basis of this assurance of the DXAFS analysis, we have performed time-resolved DXAFS measurements during the carbonylation (CO adsorption) of $[Ru_6C]$/MgO under CO/H_2 and the decarbonylation (CO desorption) of $[Ru_6C(CO)_{11}]$/MgO under vacuum.

3.2. Carbonylation Process of $[Ru_6C]$/MgO by DXAFS. Figure 3a,b shows a series of DXAFS spectra and their Fourier transforms (FT) at the Ru K-edge, respectively, during the carbonylation of $[Ru_6C]$/MgO (**1**) under CO/H_2 (26.7 kPa/ 26.7 kPa) at 523 K. The data acquisition time was 1 s, and the 1-s integrated spectra were recorded every 2.1 s. In the FT functions, three distinct peaks around 0.18, 0.21, and 0.28−0.30 nm (phase shift uncorrected) were observed, which are assigned to Ru−C−(O), Ru−O, and Ru−Ru+Ru−(C)−O form, respectively. The change in FT during the first 20 s is depicted in Figure 3c. The FT peak intensity for Ru−O bond did not change with the CO/H_2 exposure time, while the intensities of other peaks dramatically changed with the time at 523 K. The curve-fitting analysis of the FT functions at 0, 2.1, and 37.8 s is typically shown in Figure 4. The determined structural parameters are given in Table 2. The CNs of Ru−C−(O) and Ru−(C)−O for Ru carbonyls were set to be the same value in the curve-fitting analysis. At 0 s, the R and CN of Ru−Ru were 0.265 nm and 4.1, respectively. After the CO/H_2 exposure at 523 K, Ru−C−(O) and Ru−(C)−O bonds appeared at 0.185 and 0.297 nm, respectively, and the CN increased from 0 to 1.0 at 2.1 s and 1.9 at 37.8 s. At 37.8 s, the *R* of Ru−Ru increased from 0.265 to 0.271 nm, indicating an expansion of the cluster framework as mentioned above.

TABLE 2: Structural Parameters for [Ru_6Cl]/MgO(1), [$Ru_6C(CO)_{11}$]/[MgO(4), and Three Intermediates (2), (3), and (5) in the Carbonylation and Decarbonylation Processes Obtained by DXAFS

abs.-scat	CN	R/0.1 nm	$\sigma^2/10^{-5}$ nm^2
Cluster (**1**) ($\Delta E_0 = -5.3$ eV, $R_f = 2.8\%$, R range = 0.16−0.32 nm)			
Ru−Ru	4.1 ± 0.5	2.65 ± 0.02	10.9
Ru−O	0.9 ± 0.5	2.01 ± 0.03	13.9
Intermediate (**2**) produced from (**1**) under CO/H_2 (2.1 s, 523 K) ($\Delta E_0 = -6.0$ eV, $R_f = 3.4\%$, R range = 0.10−0.32 nm)			
Ru−Ru	3.5 ± 0.7	2.65 ± 0.02	10.9
Ru−C	1.0 ± 0.4	1.85 ± 0.03	7.6
Ru−(C)−O	1.0 ± 0.4	2.97 ± 0.04	8.0
Ru−O	1.1 ± 0.5	2.05 ± 0.03	14.9
Cluster (**4**) produced from (**1**) under CO/H_2 (37.8 s, 523 K) ($\Delta E_0 = -7.0$ eV, $R_f = 4.5\%$, R range = 0.10−0.32 nm)			
Ru−Ru	3.4 ± 0.7	2.71 ± 0.02	13.4
Ru−C	1.9 ± 0.4	1.87 ± 0.03	7.6
Ru−(C)−O	1.9 ± 0.4	2.97 ± 0.04	8.0
Ru−O	1.0 ± 0.5	2.08 ± 0.04	14.9
Intermediate (**3**) produced from (**4**) under vacuum (5 min, 573 K) ($\Delta E_0 = -8.0$ eV, $R_f = 4.9\%$, R range = 0.10−0.32 nm)			
Ru−Ru	3.4 ± 0.7	2.69 ± 0.02	14.0
Ru−C	1.1 ± 0.4	1.86 ± 0.02	8.1
Ru−(C)−O	1.1 ± 0.4	2.96 ± 0.03	9.2
Ru−O	0.9 ± 0.6	2.04 ± 0.04	15.0
Intermediate (**5**) produced from (**4**) under vacuum (12 min, 573 K) ($\Delta E_0 = -8.9$ eV, $R_f = 2.8\%$, R range = 0.16−0.32 nm)			
Ru−Ru	3.3 ± 0.6	2.69 ± 0.02	12.4
Ru−O	1.0 ± 0.4	2.07 ± 0.04	15.0

Curve-fitting analyses of the series of time-resolved DXAFS data (Figure 3) under CO/H_2 at 423, 473, and 523 K were performed, and the obtained structural parameters (CN and R) were plotted as a function of the CO/H_2 exposure time in Figure 5 a,b. Residual factors for the curve fitting of all the data were smaller than 10%. There was a definite time delay between the CO adsorption and the Ru−Ru bond change in Figure 5. The CN of Ru−CO at 423 K increased from 0 to 0.7 at 2.1 s, whereas the R of Ru−Ru changed little, as shown in Figure 5a,b. The CN of Ru−CO increased to about half of the value at saturation after 4.2 s, but the R of Ru−Ru did not yet change significantly at 423 K. After 4.2 s, the R rapidly increased to 0.269 nm, and the bond expansion to 0.269 nm was completed in 10.5 s at 423 K. In the increase of CN, there was a break at 4.2 s, followed by a gentle slope over 35 s. On the other hand, the slope of the increase in the R at 423 K changed around 10.5 s, followed by a gentle increase from 0.269 to 0.271 nm over 30 s. Thus it is reasonable that we postulate the existence of two intermediate structures [$Ru_6C(CO)_6$] with Ru−Ru distances of 0.265 nm (**2**) and 0.269 nm (**3**), respectively, during the carbonylation of [Ru_6C]/MgO. The rates of carbonylation and bond expansion were promoted with increasing temperature as shown in Figure 5a,b.

The number of CO molecules adsorbed per [Ru_6C] cluster was also determined volumetrically by CO adsorption measurements. Figure 6 is the plot of the amount of adsorbed CO against the exposure time, where the change of the CNs determined by DXAFS was almost the same as that of the CO uptake measured volumetrically. At first, six CO molecules adsorbed on a [Ru_6C] cluster (**1**). After the formation of the second intermediate [$Ru_6C(CO)_6$] (**3**) with the Ru−Ru bond distance of 0.269 nm, CO molecules further adsorbed on the expanded cluster, and eventually the more expanded cluster structure [$Ru_6C(CO)_{11}$] (**4**) with the Ru−Ru bond of 0.271 nm and 11 CO ligands was formed after 37.8 s at 423 K.

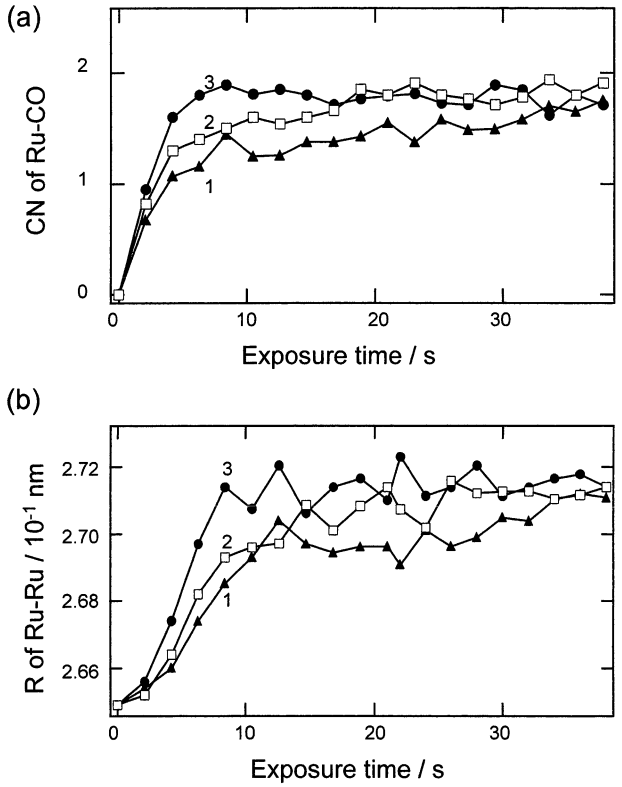

Figure 5. CN of Ru−CO (a) and the bond distances (R) of Ru−Ru (b) as a function of the CO/H_2 exposure time at 423 K. 1: ▲, 473 K. 2: □, 523 K. 3: (●). P_{co} = 26.7 kPa; P_{H2} = 26.7 kPa; Cat. weight = 90 mg.

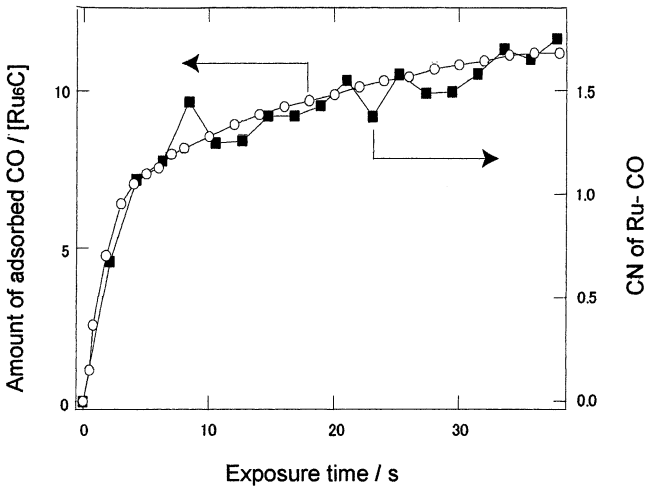

Figure 6. CN of Ru−CO determined by DXAFS, and the amount of adsorbed CO per [Ru_6C] measured volumetrically as a function of the CO/H_2 exposure time.

3.3. Decarbonylation Process of [$Ru_6C(CO)_{11}$]/MgO. The time scale and sequence of the structural change in the decarbonylation process from [$Ru_6C(CO)_{11}$]/MgO (**4**) to [Ru_6C]/MgO (**1**) under vacuum were also investigated by the DXAFS technique. Figure 7a,b shows a series of DXAFS spectra and their Fourier-transformed functions at the Ru K-edge during the decarbonylation at 573 K. Data acquisition time was 2.0 s, and the spectra were recorded every 3.0 s. The CO/H_2 gases in the in situ DXAFS cell were evacuated at 0 s after the first XAFS spectrum was recorded. In the series of FT functions, the intensities of the peaks around 0.18 and 0.28−0.30 nm (phase shift uncorrected) for Ru−C−(O) and Ru−Ru+Ru−(C)−O changed remarkably with evacuation time, while the peak

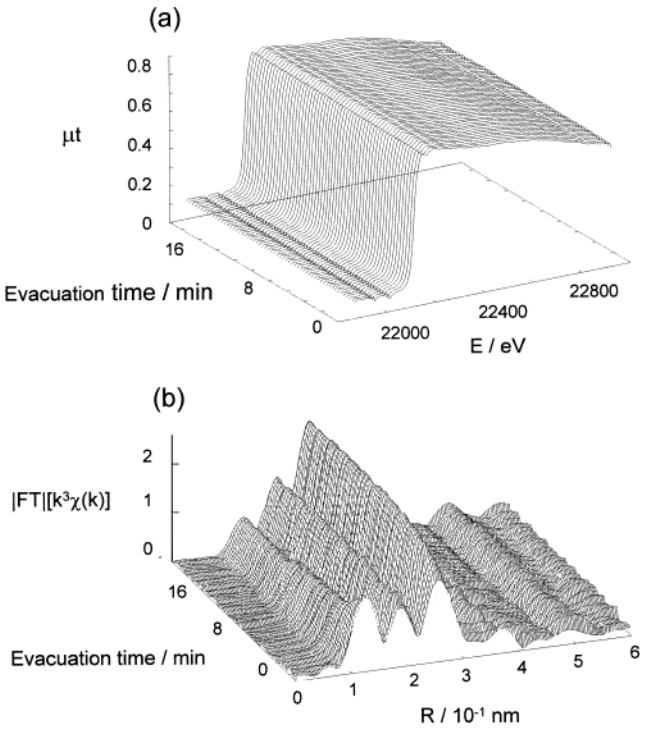

Figure 7. A series of DXAFS spectra (a) and their Fourier-transformed functions (b) at the Ru K-edge during the decarbonylation of $[Ru_6C(CO)_{11}]$/MgO (**4**) under vacuum at 573 K.

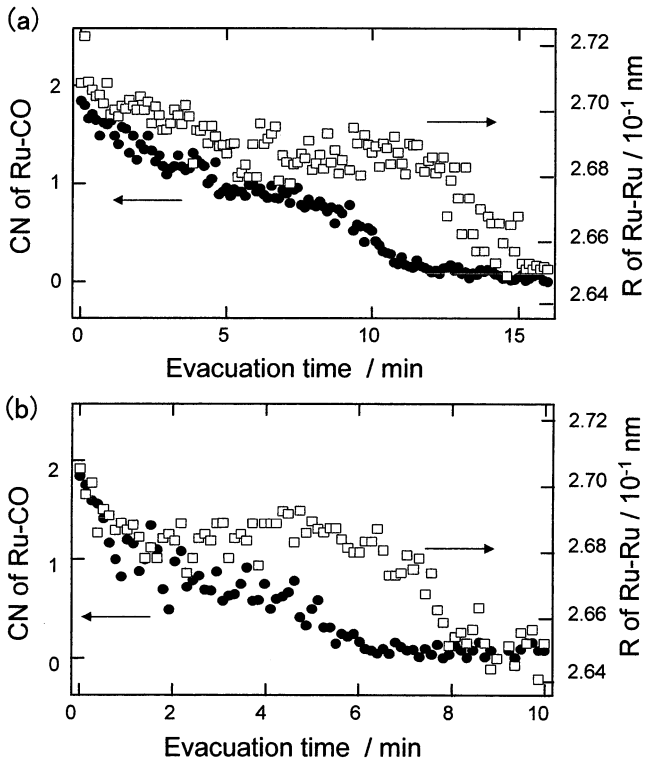

Figure 8. CN of Ru−CO (●) and the bond distances (*R*) of Ru−Ru (□) during the decarbonylation processes at 573 K (a) and 623 K (b).

intensity for Ru−O did not change over the experiments. Curve-fitting analyses for the time-resolved DXAFS data in the decarbonylation processes at 623 and 573 K were performed, and the determined structural parameters (CNs and Rs) are plotted as a function of the evacuation time in Figure 8a,b. The curve-fitting results for the samples after 5 and 12 min at 573 K are typically shown in Table 2, where the samples at 5 and

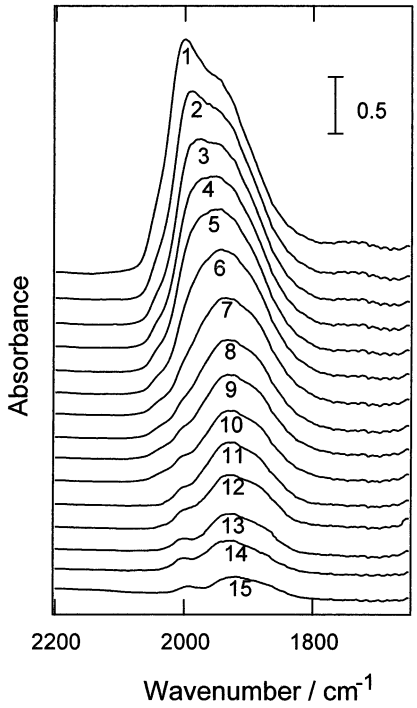

Figure 9. FT-IR spectra in the region 2250−1680 cm^{-1} in situ under vacuum after CO/H_2 reaction on $[Ru_6C]$/MgO at 573 K. 1: 0 min, 2: 0.8 min, 3: 1.6 min, 4: 2.4 min, 5: 3.2 min, 6: 4.0 min, 7: 4.8 min, 8: 5.6 min, 9: 6.4 min, 10: 7.2 min, 11: 8.0 min, 12: 8.8 min, 13: 9.6 min, 14: 10.4 min, 15: 12 min.

12 min are regarded to be two different intermediates formed during the decarbonylation at 573 K as shown in Figure 8a. The decarbonylation process was much slower than the carbonylation process. At 523 K the *R* of Ru−Ru changed a little from 0.271 to 0.269 nm in 5 min, while the CN of Ru−CO decreased to about half of the original value. The CN decreased to zero at 11 min via a plateau at 5−8 min. During this period, the *R* remained constant until 12 min. After the completion of CO desorption, the *R* of Ru−Ru began to decrease from 0.269 to 0.265 nm, and the cluster shrinkage was completed at 16 min at 573 K, as shown in Figure 8a. The stepwise feature of the decarbonylation process was also observed at 623 K in Figure 8b. At 623 K, the first structural change occurred within 2 min. The CN of Ru−CO decreased to zero at 6 min via a plateau at 2−4 min, while the *R* of Ru−Ru remained unchanged until 6 min, followed by the cluster shrinkage, which was completed at 9 min. There were definite delays of the shrinkage of the cluster framework from the complete decarbonylation at both temperatures. It is reasonable that we postulate the existence of two intermediate structures $[Ru_6C(CO)_6]$ (**3**) and $[Ru_6C]$ (**5**) with the Ru−Ru bond distance of 0.269 nm during the decarbonylation of $[Ru_6C(CO)_{11}]$/MgO (**4**).

The number of the carbonyls per cluster in the intermediates produced in the slow decarbonylation process was also estimated by FT-IR as shown in Figure 9. The peak at 1740 cm^{-1} indicates the presence of a bridge CO ligand on the $[Ru_6C(CO)_{11}]$ cluster (**4**), similar to the case of the $[Ru_6C(CO)_{16}CH_3]^-$ precursor. The change in the peak intensity approximately reproduced the change in the CN of Ru−CO. In the first step, the CO ligands on relatively cationic Ru atoms, which are probably the Ru atoms directly bound to the MgO surface through the Ru−O bonds at 0.204 nm, desorbed within 5 min at 573 K. The remaining carbonyls rapidly desorbed after 8 min in Figure 9. The similar peak positions in the spectra after 5 min indicate a uniform change in the cluster species on MgO.

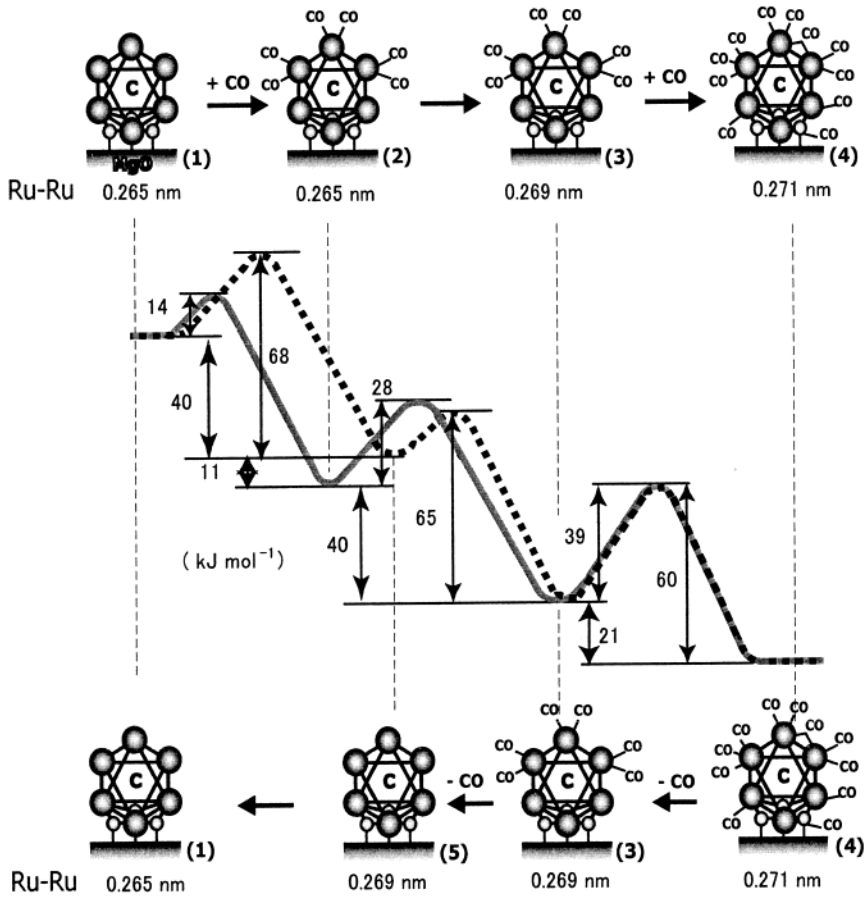

Figure 10. The energy profiles for the structural changes in the steps (1) → (4) and (4) → (1) determined by DXAFS.

TABLE 3: Activation Energies (E_a) and Pre-Exponential Factors (A) for Each Step of the Transformations of Cluster Structures

	change of Ru−Ru bond distance		change of Ru−CO bond number	
step[a]	E_a/kJ mol^{-1}	A[b]/s^{-1}	E_a/kJ mol^{-1}	A[b]/s^{-1}
(1) → (2)			14 ± 2	5.5×10^2
(2) → (3)	28 ± 3	3.1×10^4		
(3) → (4)	38 ± 4	1.0×10^7	41 ± 5	5.4×10^7
(4) → (3)	62 ± 6	2.6×10^9	59 ± 6	8.5×10^8
(3) → (5)			65 ± 7	9.3×10^9
(5) → (1)	68 ± 7	3.1×10^{10}		

[a] Refer to Figure 12. [b] 523 K.

The energy profiles for the structural changes in the carbonylation and decarbonylation processes are illustrated in Figure 10, where the activation energies for each step and the energy difference between the species are also shown as Arabic numbers in kJ mol^{-1}. We assumed that the rates were proportional to the cluster at the surface on which the dynamics event occurs.

The activation energy for the step from [Ru_6C] (Ru−Ru: 0.265 nm) (**1**) to [$Ru_6C(CO)_6$] (0.265 nm) (**2**) was determined to be 14 kJ mol^{-1} by using the rates of the increase in the CN of Ru−CO, while the activation energy for the step from [$Ru_6C(CO)_6$] (0.265 nm) (**2**) to [$Ru_6C(CO)_6$] (0.269 nm) (**3**) was determined to be 28 kJ mol^{-1} by using the rates of the increase in the *R* of Ru−Ru bond (Table 3). The activation energy for the step from [$Ru_6C(CO)_6$] (0.269 nm) (**3**) to [$Ru_6C(CO)_{11}$] (0.271 nm) (**4**) was obtained by using the rates of the increases in the CN and the *R*, independently. The values determined from the CN and the *R* were 41 and 38 kJ mol^{-1}, respectively, which agreed well with each other (Table 3). The compensation effect in the values of the activation energies and pre-exponential factors for the series of the structural transformations (**1**) → (**2**) → (**3**) → (**4**) was observed.

In the decarbonylation process, the activation energy for the step from [$Ru_6C(CO)_{11}$] (0.271 nm) (**4**) to [$Ru_6C(CO)_6$] (0.269 nm) (**3**) was determined to be 59 and 62 kJ mol^{-1} from the rates of the decreases in the CN of Ru−CO and the *R* of Ru−Ru, respectively (Table 3). Both values agreed with each other, indicating the validity of the values. The activation energy for the step from [$Ru_6C(CO)_6$] (0.269 nm) (**3**) to [Ru_6C] (0.269 nm) (**5**) was calculated to be 65 kJ mol^{-1} from the rate of the decrease in the CN. The activation energy for the step from [Ru_6C] (0.269 nm) (**5**) to [Ru_6C] (0.265 nm) (**1**) was determined to be 68 kJ mol^{-1} from the *R* (Table 3).

The carbonyls at 2004 cm^{-1} coordinated to the Ru atoms of the bottom triangle plane and the bridging carbonyl at 1740 cm^{-1} on the Ru atoms of the upper triangle plane first desorbed in the decarbonylation of [$Ru_6C(CO)_{11}$]/MgO (**4**), accompanied with a little decrease of the Ru−Ru bond distance. This is a reverse step to the step (**3**) → (**4**). The slow step (**3**) → (**4**) was also monitored by FT-IR, which revealed the appearance of the peaks at 2004 and 1740 cm^{-1}. The carbonyls in the clusters (**2**) and (**3**) revealed peaks around 1952 cm^{-1}. In addition to the six activation energies determined directly by the DXAFS, the activation energies for the other four reverse steps can also be estimated on the basis of the determined cluster structures. The decarbonylation step (**3**) → (**5**) showed a high activation energy of 65 kJ mol^{-1}, while the reverse step (**5**) → (**3**) should resemble step (**1**) → (**2**) because both steps involve the adsorption of six CO molecules without change of the Ru−Ru bond distances, 0.269 and 0.265 nm, respectively. Therefore, the activation energy for the virtual step (**5**) → (**3**) is assumed to be 14 kJ

mol^{-1}. The activation energy of the step (**5**) → (**1**) was 68 kJ mol^{-1}, while the reverse virtual step (**1**) → (**5**) can be estimated to be 28 kJ mol^{-1} because the step should resemble step (**2**) → (**3**), where the change occurs only on the Ru−Ru bond. Thus, the energy difference between clusters (**1**) and (**5**) at the surface was 40 kJ mol^{-1}. Similarly, the activation energy of the reverse step (**3**) → (**2**) may be similar to 68 kJ mol^{-1} for the step (**5**) → (**1**), and thus the energy difference between clusters (**2**) and (**3**) is regarded to be 40 kJ mol^{-1}. As a consequence, we have succeeded in determining all the activation energies for the 10 elementary processes of the cluster structure transformations at the MgO surface. This sort of information on the dynamics of the framework in a single cluster molecule at the surface as the catalytically active site was obtained by the time-resolved DXAFS technique for the first time.

4. Summary

We have shown the time scale and bond sequence and the activation energies of each step in the dynamic structural transformations through three identified intermediates at the MgO surface by means of in situ time-resolved DXAFS. The time scale and sequence of the structural dynamics may be relevant to key issues to understand the dynamic behavior of catalytically active cluster structures. The $[Ru_6C(CO)_{11}]$/MgO catalyst (**4**) is more active than the $[Ru_6C]$/MgO catalyst (**1**) for the CO/H_2 conversion to the oxygenated products. CO molecules adsorb on the expanded clusters, and the adsorbed CO molecules are consumed by reaction with H_2. But the next CO molecules can adsorb on the expanded framework before shrinkage, where a steady-state catalytic reaction is possible on the active expanded cluster framework. This study reports the full analysis of the time scale, the bond sequence, and the kinetic parameters of concerted structural changes of single cluster molecules dispersed on the surface, presenting the detail of dynamic bond information by in situ time-resolved DXAFS. The accumulated knowledge of the time-resolved observation of structural changes under the catalytic reaction conditions may give new insight into the detail of catalytic reaction mechanism and provide new concepts and strategies to develop efficient catalytic materials and systems illustrating structure dynamics and chemical design at surfaces.

Acknowledgment. This study was supported by a Grant-in-aid for the 21st Century COE Program for Frontiers in Fundamental Chemistry from the Ministry of Education, Culture, Sports, Science and Technology.

References and Notes

(1) Iwasawa, Y. *Adv. Catal.* **1987**, *35*, 187.
(2) Iwasawa, Y. *Stud. Surf. Sci. Catal*. **1996**, *101*, 21.
(3) Frahm, R. *Nucl. Instrum. Methods A* **1988**, *270*, 578.
(4) Frahm, R. *Rev. Sci. Instrum.* **1989**, *60*, 2515.
(5) Evans, J.; O'Neill, L.; Kambhampati, V. L. *J. Chem. Soc., Dalton Trans.* **2002**, 2207.
(6) Grunwaldt, J. D.; Lutzenkirchen-Hecht, D.; Richwin M.; Grundmann, S.; Clausen, B. S.; Frahm, R. *J. Phys. Chem. B* **2001**, *105*, 5161.
(7) Richwin, M.; Zaeper, R.; Lutzenkirchen-Hecht, D.; Frahm, R. *J. Synchrotron Radiat*. **2001**, *8*, 354.
(8) Webb, S. M.; Gaillard, J. F.; Jackson B. E. *J. Synchrotron Radiat*. **2001**, *8*, 943.
(9) Clausen, B. S.; Grabak, L.; Steffensen, G.; Hansen, P. L.; Topsoe, H. *Catal. Lett.* **1999**, *20*, 23.
(10) Grunwaldt, J.-D.; Molenbroek, A. M.; Topsoe, N.-Y.; Topsoe, H.; Clausen, B. S. *J. Catal*. **2000**, *194*, 452.
(11) Sun, M.; Burgi, T.; Cataneo, R.; Prins, R. *J. Catal*. **2001**, *197*, 172.
(12) Cimini, F.; Prins, R. *J. Phys. Chem. B* **1997**, *101*, 5277.
(13) Prestipino, C.; Berlier, G.; Llabres, F. X.; Xamena, I.; Spoto, G.; Bordiga, S.; Zecchina, A.; Tirmes Palomino, G.; Yamamoto, T.; Lamberti, C. *Chem. Phys. Lett.* **2002**, *363*, 389.
(14) Geantet, C.; Soldo, Y.; Gkasson, C.; Matsubayashi, N.; Lacroix, M.; Proux, O.; Ulrich, O.; Hazemann, J. L. *Catal. Lett.* **2001**, *73*, 2.
(15) Neylon, M. K.; Marshall, C. L.; Kropf, A. J. *J. Am. Chem. Soc.* **2002**, *124*, 5457.
(16) Matsushita, T.; Phizackerley, R. P. *Jpn. J. Appl. Phys.* **1981**, *20*, 2223.
(17) Flank, A. M.; Fontaine, A.; Jucha, A.; Lemonnier, M.; Williams, C. *J. Phys., Lett.* **1982**, *43*, L315.
(18) Rumpg, H.; Janssen, J.; Modrow, H.; Winkler, K.; Hormes, J. *J. Solid State Chem.* **2002**, *163*, 158.
(19) Dartyge, E.; Fontaine, A.; Jucha, A.; Sayers, D. *EXAFS and Near Edge Structure III*; Springer-Verlag: Berlin, 1984.
(20) *X-ray Absorption: Principles, Applications, Techniques of EXAFS, SEXAFS and XANES*; Koningsberger, D. C., Prins, R., Eds.; Wiley: New York, 1988.
(21) *X-ray Absorption Fine Structure for Catalysts and Surfaces*; Iwasawa, Y.; Ed.; World Scientific: Singapore, 1996.
(22) Fontaine, A.; Dartyge, E.; Itie, J. P.; Jucha, A.; Polian, A.; Tolentino, H.; Tourillon, G. *Top. Curr. Chem*. **1989**, *151*, 179.
(23) Couves, J. W.; Thomas, J. M.; Waller, D.; Jones, R. H.; Dent, A. J.; Derbyshire, G. E.; Greaves, G. N. *Nature* **1991**, *354*, 465.
(24) Sanker, G.; Thomas, J. M.; Waller, D.; Couves, J. W.; Catlow, C. R. A.; Greaves, G. N. *J. Phys. Chem*. **1992**, *96*, 7485.
(25) Ressler, T.; Hagelstein, M.; Hatje, U.; Metz, W. *J. Phys. Chem. B* **1997**, *101*, 6680.
(26) Hilbrandt, N.; Frahm, R.; Martin, M. *J. Phys. IV* **1997**, *7*, 727.
(27) Fiddy, S. G.; Newton, M. A.; Dent, A. J.; Salvini, G.; Corker, J. M.; Turin, S.; Campbell, T.; Evans, J. *J. Chem. Soc., Chem. Commun*. **1999**, 851.
(28) Dent, A. J.; Evans, J.; Newton, M.; Corker, J.; Russell, A.; Abdul Rahman, M. B.; Fiddy, S.; Mathew, R.; Farrow, R.; Salvini, G.; Atkinson, P. *J. Synchrotron Radiat*. **1999**, *6*, 381.
(29) Yamaguchi, A.; Shido, T.; Inada, Y.; Kogure, T.; Asakura, K.; Nomura, M.; Iwasawa, Y. *Catal. Lett.* **2000**, *68*, 139.
(30) Yamaguchi, A.; Suzuki, A.; Shido, T.; Inada, Y.; Asakura, K.; Nomura, M.; Iwasawa, Y. *Catal. Lett*. **2001**, *71*, 203.
(31) Yamaguchi, A.; Shido, T.; Inada, Y.; Kogure, T.; Asakura, K.; Nomura, M.; Iwasawa, Y. *Bull. Chem. Soc. Jpn*. **2001**, *74*, 801.
(32) Fiddy, S. G.; Newton, M. A.; Campbell, C. T.; Corker, J. M.; Turin, S.; Evans, J.; Dent, A. J.; Harvey, I.; Salvini, G. *Chem. Commun.* **2001**, 445.
(33) Newton, M. A.; Burnaby, D. G.; Dent, A. J.; Diaz-Moreno, S.; Evans, J.; Fiddy, S. G.; Neisius, T.; Pascaralli, S.; Turin, S. *J. Phys. Chem. A* **2001**, *105*, 5965.
(34) Yamaguchi, A.; Suzuki, A.; Shido, T.; Inada, Y.; Asakura, K.; Nomura, M.; Iwasawa, Y. *J. Phys. Chem. B* **2002**, *106*, 2415.
(35) Dent, A. J. *Top. Catal*. **2002**, *18*, 27.
(36) Evans, J.; O'Neill, L.; Kambhampati, V. L.; Rayner, G.; Turin, S.; Genge, A.; Dent, A. J.; Neisius, T. *J. Chem. Soc., Dalton Trans.* **2002**, 2207.
(37) Carlo, L.; Carmelo, P.; Francesca, B.; Luciana, C.; Silvia, B.; Giuseppe, S.; Adriano, Z.; Sofia, D. M.; Barbara, C.; Marco, G.; Andrea, M.; Diego, C.; Sandro, V.; Giuseppe, L. *Angew. Chem., Int. Ed*. **2002**, *41*, 2247.
(38) Meneau, F.; Sankar, G.; Morgante, N.; Winter, R.; Catlow, C. R. A.; Greaves, G. N.; Thomas, J. M. *Faraday Discuss.* **2003**, *122*, 203.
(39) Tourillon, G.; Dartyge, E.; Dexpert, H.; Fontaine, A.; Jucha, A.; Lagarde, P.; Sayers, De. *J. Electroanal. Chem.* **1984**, *178*, 357.
(40) Bazin, D.; Dexpert, H.; Lagarde, P.; Bournonville, P. *J. Catal*. **1988**, *110*, 209.
(41) Iwasawa, Y. *J. Catal*. **2003**, *216*, 165.
(42) Suzuki, A.; Inada, Y.; Yamaguchi, A.; Chihara, T.; Yuasa, M.; Iwasawa, Y. *Angew. Chem., Int. Ed.* **2003**, *42*, 4795.
(43) Izumi, Y.; Chihara, T.; Yamazaki, H.; Iwasawa, Y. *J. Phys. Chem*. **1994**, *98*, 594.
(44) Izumi, Y.; Iwasawa, Y. *CHEMTECH* **1994**, *24*, 20.
(45) Izumi, Y.; Chihara, T.; Yamazaki, H.; Iwasawa,Y. *J. Am. Chem. Soc*. **1993**, *115*, 6462.
(46) Hagelstein, M.; Ferrero, C.; Sanchez del, R.; Hatje, U.; Ressler, T.; Metz, W. *Physica B* **1995**, *208*, 223.
(47) Stern, E. A.; Newville, M.; Ravel, B.; Yacoby, Y.; Haskel, D. *Physica B* **1995**, *208*, 117.
(48) Newville, M.; Livins, P.; Yacoby, Y.; Stern, E. A.; Rehr, J. J. *Phys. Rev. B* **1993**, *47*, 14126.
(49) Ankudinov, A. L.; Ravel, B.; Rehr, J. J.; Conradson, S. D. *Phys. Rev. B* **1998**, *58*, 7565.
(50) Stern, E. A. *Phys. Rev. B* **1993**, *48*, 9825.